



# The effect of friction stir processing on the hydrogen susceptibility of AA5083 specimens after hydrogen cathodic charging

Ioannis G. Papantoniou<sup>1,2</sup> · Panagiotis Karmiris-Obratański<sup>1,3</sup> · Beata Leszczyńska-Madej<sup>4</sup> · Dimitrios E. Manolakas<sup>1</sup>

Received: 23 November 2022 / Accepted: 19 January 2023 / Published online: 7 February 2023  
© The Author(s) 2023

## Abstract

The present study investigated the effect of hydrogen on the mechanical degradation of friction stir processed (FSPed) 5083 aluminum alloy by intense hydrogen cathodic charging (HCC). The effect of different numbers of FSP passes was investigated: 3 and 8 passes, respectively. Hydrogen-charged and uncharged specimens were subjected to tensile testing and microhardness evaluation analysis, and were examined through optical microscopy, focus variation microscopy (FVM), and scanning electron microscopy (SEM) both on the microstructure and fracture zone. The results showed that the FSP process introduced a refined microstructure with finer grains. This led to an improved mechanical response during tension tests of the uncharged specimens; the energy absorption increased from 85 MJ/m<sup>3</sup> of the base material to 94 MJ/m<sup>3</sup> and 97 MJ/m<sup>3</sup> for the 3 and 8 FSP passes, respectively. The introduction of hydrogen through the HCC process led to a more brittle mechanical response with a decrease in the energy absorption capability for all the charged specimens. The more prone specimen was the 8 FSP passes specimen where the energy absorption dropped by 20% and 71% for the two different charging current densities. The 3 FSP passes specimen presented a reduction of energy absorption of 4% and 18%, respectively, where the base material presented a reduction of 8% and 14%, respectively. This brittle response is also evident from the microhardness testing where the hydrogen charging led to increased surface hardness values. The 3 FSP passes specimen presented a better mechanical response with respect to the base material specimen (and the 8 FSP passes specimen) for all the charging conditions, and this led to the conclusion that a small number FSP surface modification could be a beneficial surface modification process as it improves the mechanical response of the material and is not significantly affected by hydrogen charging environments.

**Keywords** Friction stir processing · Hydrogen embrittlement · Hydrogen cathodic charging · AA5083 · Fracture analysis, Microstructure

## 1 Introduction

The friction stir process (FSP), based on friction stir welding (FSW), is an emerging processing technique for localizing microstructures in near surface layers of processed metal components [1, 2]. In this technique, high temperatures and high strain rates can be applied to introduce microstructural modification [3] and develop nanocomposite materials [4, 5]. As an eco-friendly and solid-state surface composite fabrication technique, FSP is used in a wide range of industries such as automotive, energy, aerospace, aviation, and shipping. In FSP, a cylindrical tool with a shoulder and probe (pin) traverses the surface of the workpiece after being inserted into a metallic plate [6]. The tool shoulders scrape against the surface of the plate, creating frictional heat that

✉ Ioannis G. Papantoniou  
ipapanto@central.ntua.gr

<sup>1</sup> School of Mechanical Engineering - Laboratory of Manufacturing Technology, National Technical University of Athens, Athens, Greece

<sup>2</sup> Department of Naval Architecture, School of Engineering, University of West Attica, 12243 Egaleo, Greece

<sup>3</sup> Faculty of Mechanical Engineering and Robotics, Department of Manufacturing Systems, AGH University of Science and Technology, Cracow, Poland

<sup>4</sup> Department of Materials Science and Non-Ferrous Metals Engineering, Faculty of Non-Ferrous Metals, AGH University of Science and Technology, 30-059 Cracow, Poland

softens the underneath material, which is severely deformed by the revolving pin at high strain rates [7].

One of the most commonly used materials for structural applications in the abovementioned industrial sectors is aluminum and its alloys due to its superior formability, high specific strength, and corrosion resistance [8]. The FSP method was investigated by Mishra et al. [9] in order to achieve high strain rate superplasticity in AA7075. The results show that FSP can achieve optimum superplasticity at  $1 \times 10^{-2} \text{ s}^{-1}$  and 490 °C. Johannes and Mishra [10] used the same alloy to investigate the multi-pass effect on the superplasticity using up to 4 passes. Although by using multiple passes, superplasticity can be achieved in larger areas, the results showed that a single pass can achieve larger elongation. A study conducted by Yadva and Bauri [11] found that FSP can improve the mechanical properties of cast aluminum. According to the results, despite the notable increase in strength of the friction stir processed material, the ductility was not significantly reduced, and the hardness increased by about 34%. The microstructure and microhardness of pure aluminum modified by FSP were investigated by Gan et al. [12]. According to their findings, the microhardness in the stir zone (SZ) decreased due to the produced heat, but they achieved ultra-fine grain size. Using constant speed and feed, Senthilkumar et al. [13] increased the number of passes in the same direction. Due to recrystallization, it is possible to minimize tunnel voids at stir zones by increasing the number of passes with the specific rotational speed. The effect of the tools' geometry on the superplasticity was investigated by Patel et al. [14] using square, pentagon, and hexagon pins. Their findings showed that square pins were the most effective in achieving uniform microhardness and fine grains in the SZ, as well as achieving 227% uniform elongation on the gage of an AA7075 alloy. The fatigue properties of aluminum alloys were improved due to ultra-fine grains (UFG) achieved by FSP [15, 16]. Wang et al. [17] investigated the grain size effect on the mechanical properties by analyzing the UFG microstructure of pure aluminum modified by FSP. By analyzing the strengthening mechanisms during tensile deformation, it was discovered that Hall-Petch relationships could be divided into three stages as grain size decreased from coarse to UFG. The first stage had a grain size higher than 1.2  $\mu\text{m}$ , the second stage had a grain size between 0.9 and 1.2  $\mu\text{m}$ , and finally, the third stage had a grain size smaller than 0.9  $\mu\text{m}$ . A novel vibration-assisted FSP/FSW method was presented by Bagheri et al. [18] in order to increase the mechanical characteristics. The results show that using mechanical vibration during friction stir methods can enmeshed the dislocation generation and movement, decreased grain size, improve corrosion resistance, and improve mechanical properties [19]. Abbasi et al. [20] performed experimental and simulation investigation on the dynamic recrystallization

process during FSW of AZ91 magnesium alloy by using a two-dimensional cellular automaton model. It was found that when vibration frequency is increased, nucleation begins earlier, the incubation period decreases, and the percentage of recrystallization decreases.

The degradation of mechanical properties caused by hydrogen embrittlement (HE) is a long-standing problem for structural materials [21, 22]. Due to the recent demand for hydrogen energy equipment, the problem is becoming increasingly significant, particularly for high-strength steel and aluminum alloys [23]. Aluminum alloys can absorb hydrogen when exposed to watery conditions, air saturated with water vapor, and water vapor combined with other gases like nitrogen, argon, or dihydrogen [24]. The effect of hydrogen embrittlement on the mechanical properties of AA7075 was investigated by Tanano [25]. A striation-like pattern during fracture can be attributed to hydrogen interaction with grain boundaries [26]. A relationship between tempering and HE of AA7520 was presented by Kumar and Namboodhiri [27]. According to their findings, air-cooled duplex aged alloy had the highest resistance to hydrogen embrittlement, followed by as-received (T6 condition) and water-quenched duplex aged alloy. The difference between gas phase hydrogen and environmentally HE in high-purity aluminum was studied by Scully et al. [28]. They proposed a model in order to understand the physical mechanism that occurs during embrittlement. A popular method for enhancing decohesion is hydrogen-enhanced decohesion (HEDE) [29, 30] which relies on the hydrogen-induced reduction of cohesive interfaces. In other words, hydrogen atoms that gather at sites of high triaxial stress will weaken the bonds between metal atoms and cause fractures. An investigation of the hydrogen susceptibility of 5083 aluminum alloy after cold rolling was performed by Georgiou, Celis, and Panagopoulos [31]. They found that on the surface layers of hydrogen-charged samples, brittle transcrystalline cleavages were observed along with ductile intergranular fractures. In contrast, only ductile intergranular fractures were observed at the bulk of the alloy. A numerical simulation model considering the tensile behavior of AA2024-T3 exposed to HE was proposed by Vasco et al. [32]. By incorporating both corrosion damage and corrosion-induced HE, it is demonstrated that this method can accurately predict the tensile performance of pre-corroded specimens. Safyari et al. [33] exposed AA7075 series to HE and discovered that resistance to HE is achieved by controlling the distribution of soluble second-phase particles, resulting in lower hydrogen content at dislocations. Finally, the same authors investigated the HE mechanism in high-strength aluminum alloys [34] based on inclusions of coherent or incoherent dispersoids. It was found that the presence of coherent Al<sub>3</sub>Zr dispersoids in the matrix significantly improved the alloy's HE resistance, although hydrogen trapped by misfit dislocations leads

to a decrease in elastic strain caused by lattice misfit on  $\text{Al}_{18}\text{Mg}_2\text{Cr}_3$  dispersoids.

Up to this point, despite the rapid increase of FSP applications for the refinement of aluminum alloys, the hydrogen embrittlement phenomenon in friction stirred processed (FSPed) specimens has not been studied. The aim of the present paper is the investigation of hydrogen embrittlement in FSPed specimens of AA5083. Thus, FSPed specimens with a different number of passes were subjected to electrolytic hydrogen cathodic charging (HCC). Despite the general approach of using mild HCC parameters to minimize surface damage, in the present study, intense charging conditions were employed in order to examine the response of the refined microstructures to intense surface blistering effects and simultaneous hydrogen diffusion. Charged and uncharged specimens were subjected to tensile testing and microhardness evaluation analysis and were examined through optical microscopy, focus variation microscopy (FVM), and scanning electron microscopy (SEM) both on the microstructure and fracture zone.

## 2 Materials and methods

### 2.1 Materials

As the base material, 6-mm-thick plates of aluminum alloy AA5083-H111 were applied. AA5083 is a non-heat treatable aluminum alloy widely employed in the transportation, marine, and chemical industries. It has excellent corrosion resistance in seawater atmospheres as well as high formability in soft tempers. Table 1 presents the chemical composition of AA5083.

### 2.2 FSP and specimen preparation

The FSP experiments were carried out by the use of a modified milling machine. Figure 1a shows a graphical representation of the friction stir process. The friction stir processing tool was made from heat-treated tool steel. The shoulder of the tool was flat with a diameter of 22 mm. The pin of the tool was cylindrical with right-handed thread, 4 mm diameter and 5 mm height. The applied operational parameters were 1000 rpm rotational speed combined with 13 mm/min transverse speed. Those parameters lead to high heat input and intense plastic deformation and were projected according to literature to present the optimum material mixing for AA5083 friction stir processing [4]. Three and 8 FSP passes

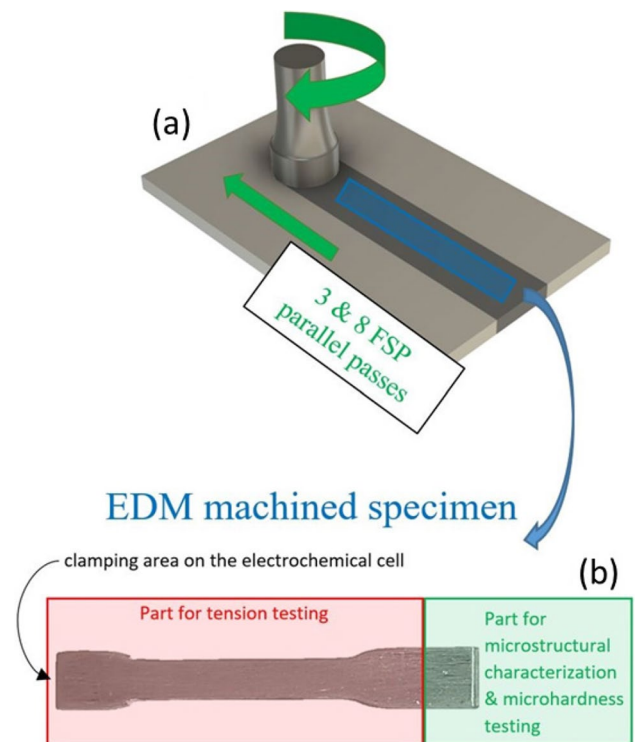


**Fig. 1** **a** Graphical representation of the FSP processing. **b** Specimen geometry: the left part was used for mechanical testing, whereas the right part was used for microstructural characterization and microhardness testing

were carried in the same direction and without allowing the samples to cool to room temperature between passes. The eight FSP passes may not be industrially cost-effective, but were chosen in the present study in order to investigate intense operational parameters [35].

Following the completion of the FSP procedure, dogbone specimens from the stir zone were machined using electro discharge machining. Particular importance was given so that the full gage length of the specimens was part of the stir zone. Furthermore, 2 mm was machined from the upper surface of the dogbone specimens in order to eliminate the introduced surface roughness and also to avoid the “flow arm” area. The “flow arm” consists of thermomechanically affected material, which is moved from the retreating side of the stir zone and is transferred to the advancing side. Thus, the microstructure in this thin surface area is not significantly affected from the process. The obtained dogbone specimens had length ( $L_c$ ) 35 mm and cross-section of 6 mm gage width and 4 mm

**Table 1** Chemical composition of AA5083-H11

| Mg  | Mn  | Fe  | Si  | Cu  | Zn   | Cr  | Ti   | Al  |
|-----|-----|-----|-----|-----|------|-----|------|-----|
| 4.5 | 0.5 | 0.4 | 0.4 | 0.1 | 0.25 | 0.2 | 0.15 | Bal |

thickness. Finally, various SiC papers were used to grind all specimens with progressively finer finishes, and finishing papers of 2000 grit were used to ensure a similar surface topography.

### 2.3 Hydrogen cathodic charging

Hydrogen was introduced into the dogbone specimens by electrolytic cathodic charging (HCC) [36]. This technique applies electrolytic cathodic charging to simulate the hydrogen adsorption and diffusion into the FSPed specimens described above. This procedure was performed in a solution consisting of 30 g/L NaCl and 3 g/L  $\text{NH}_4\text{SCN}$  electrolytes. The hydrogen charging time was kept constant at 8 h in all the experiments. Two different charging current densities were studied: 50 mA/cm<sup>2</sup> and 80 mA/cm<sup>2</sup>. The 50 and 80 mA/cm<sup>2</sup> are significantly intense conditions for HCC of aluminum alloys, but those extreme conditions could provide a correlation of the modified microstructures to hydrogen diffusion and blistering effects. Table 2 provides a summary of the process parameters.

After the hydrogen charging process, the specimens were cut in two parts as illustrated in Fig. 1b. The first part was used for mechanical testing, while the second smaller part was used for microstructural characterization and microhardness testing.

### 2.4 Microstructural characterization

Examination of the microstructure of the samples before and after HE was performed by means of Olympus GX51 light microscopy and Hitachi SU-70 scanning electron microscopy along with EDS analysis of the chemical composition in micro-areas.

**Table 2** Process parameters

| Set of specimens | Charging current density (mA/cm <sup>2</sup> ) | Number of FSP passes | Transverse speed (mm/min) | Rotational speed (rpm) |
|------------------|--|----------------------|---------------------------|------------------------|
| A11              | No charging                                    | 0                    | No FSP                    | No FSP                 |
| A12              | 50   | 0                    |                           |                        |
| A13              | 80   | 0                    |                           |                        |
| A21              | No charging                                    | 3                    | 13                        | 1000                   |
| A22              | 50   | 3                    |                           |                        |
| A23              | 80   | 3                    |                           |                        |
| A31              | No charging                                    | 8                    |                           |                        |
| A32              | 50   | 8                    |                           |                        |
| A33              | 80   | 8                    |                           |                        |

### 2.5 Mechanical characterization

Tensile testing experiments were carried out immediately after HCC in order to minimize the loss of hydrogen. The tests were performed in a universal testing machine (Instron 4482) at room temperature and ambient air and with a constant strain rate of  $7 \times 10^{-4} \text{ s}^{-1}$ . From the load–displacement acquired data, the stress–strain curves were created. From the stress–strain curves, the energy absorption until failure was calculated and the yield strength was defined. The given values presented are the mean value of three independent experiments.

### 2.6 Microhardness

This subsection is aimed at defining the interrelationship between the material microstructure, hardness, and the influence of HE. Analysis of the microhardness distribution of specimens was correlated with microstructural observations. An automated DuraScan 80 G5 (Struers) was used to evaluate the microhardness distribution pattern. The measuring force is applied, lasts between 2 and 8 s, and the test force is maintained for between 10 to 15 s following the force's removal. The indentation's diagonal lengths are measured, and the arithmetic mean is calculated. For each specimen, 90 intends were conducted using a load of 0.1 kgf according to EN ISO 14577-1:2005. There were 6 rows with 15 measurements in each row, and the distance between each measurement was 0.3 mm. It has been estimated that the microhardness of the 5083 Al alloy substrate is about 85 HV0.1 [37].

## 3 Results and discussion

### 3.1 Microstructural characterization

Figure 2 depicts the macrographs of cross-section in near surface areas of specimens with and without HCC process. Figure 2 a, d, and g present the near surface microstructures for the as-received (no FSP) specimen, and the 3 and 8 FSP passes specimens, respectively. As it is observed, the FSPed specimens introduced a significant refinement in the microstructure. After the application of FSP, the average grain size was decreased from 22  $\mu\text{m}$  (measured from Fig. 2a) to 6  $\mu\text{m}$  after 3 FSP passes (measured from Fig. 2d) and to 4  $\mu\text{m}$  after 8 FSP passes (measured from Fig. 2g). It is worth mentioning that after 8 FSP passes, the microstructure on the cross-section is more homogeneous than after 3 FSP passes (Fig. 2d–i).

Changes in the microstructure during FSP are related to both the healing and recrystallization processes (static and dynamic), as well as the refinement of second-phase



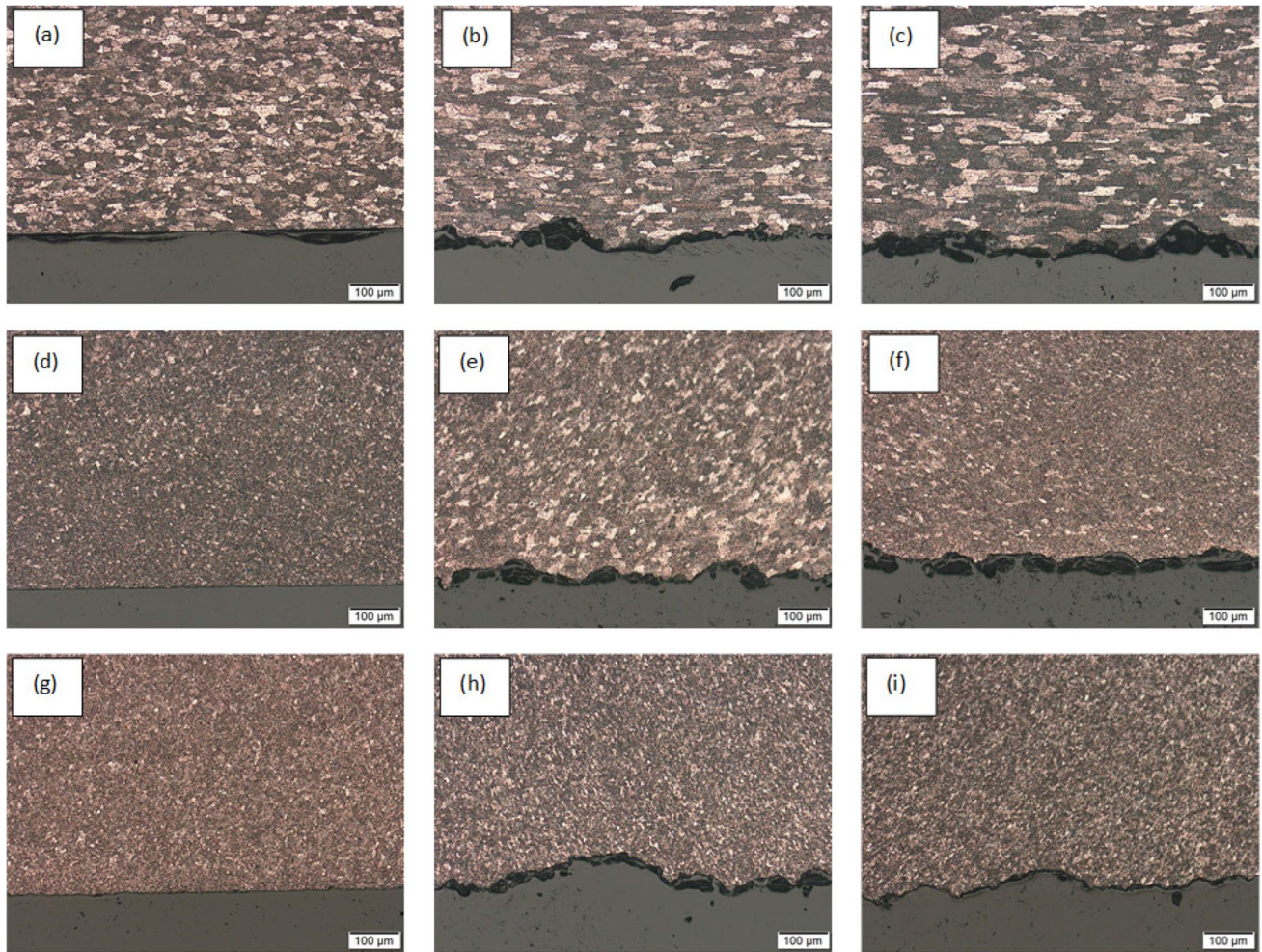


**Fig. 2** Surface cross-section micrographs of specimens: as-received without FSP, **a** no HCC (A11), **b** 50 mA/cm<sup>2</sup> (A12), **c** 80 mA/cm<sup>2</sup> (A13); 3 FSP passes, **d** no HCC (A21), **e** 50 mA/cm<sup>2</sup> (A22), **f** 80 mA/

cm<sup>2</sup> (A23); 8 FSP passes, **g** no HCC (A31), **h** 50 mA/cm<sup>2</sup> (A32), **i** 80 mA/cm<sup>2</sup> (A33)

particles. Furthermore, the microstructure in the post-treatment zone results from the material flow in addition to the temperature and deformation gradient, leading to compaction and homogenization of the material. The evolution of the microstructure in the processing zone takes place in three stages: stage I involves changes in the volume of the material in the shear layer around the pin and below the tool shoulder (nucleation and grain growth); stage II consists of modifications due to the simultaneous effects of temperature and strain (dynamic healing and dynamic recrystallization); stage III takes into account the evolution associated with the effects of temperature (static healing, static recrystallization, and grain growth) [38]. When aluminum alloys are strained at elevated temperatures, they can experience work hardening and flow softening that results from dynamic recovery (DRV), dynamic recrystallization (DRX), or dynamic precipitation transformations [39, 40]. Due to the high stacking fault energy of aluminum alloys, dynamic recovery (DRV)

was more likely to occur than dynamic recrystallization (DRX) [41].

Micrographs of Fig. 2 b, e, and h present the near surface microstructures for the specimens with 50 mA/cm<sup>2</sup> HCC current density and micrographs of Fig. 2 c, f, and i, respectively, present the near surface microstructures for the specimens with 80 mA/cm<sup>2</sup> HCC current density. No significant defects can be observed from the microscopical investigation (near surface large voids or cracks). The extensive blistering effects led to high roughness surfaces with different morphologies. The larger grains of the as-received specimens presented high amplitude blisters (Fig. 2b, c). The more refined microstructure of the 3 and 8 FSP passes specimens led to smaller blisters and thus smoother surfaces. Specifically, the 8 FSP specimens introduced smoother surface with a waviness profile (Fig. 2h, i).

The intense charging conditions of the HCC process introduced intense blistering effects that led to thickness

reduction of the dogbone specimens. Figure 3 presents the thickness reduction values for all the specimens. The 80 mA/cm<sup>2</sup> charging current led to significantly higher thickness reduction values for all the specimens with respect to the lower 50 mA/cm<sup>2</sup>. The most important outcome is that the 3 and 8 FSP passes specimens presented higher thickness reduction values for both HCC current densities. This is an indication that the refined microstructure of

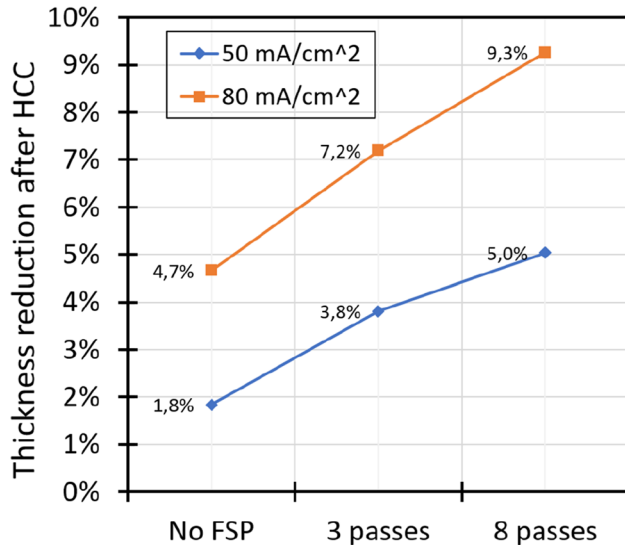


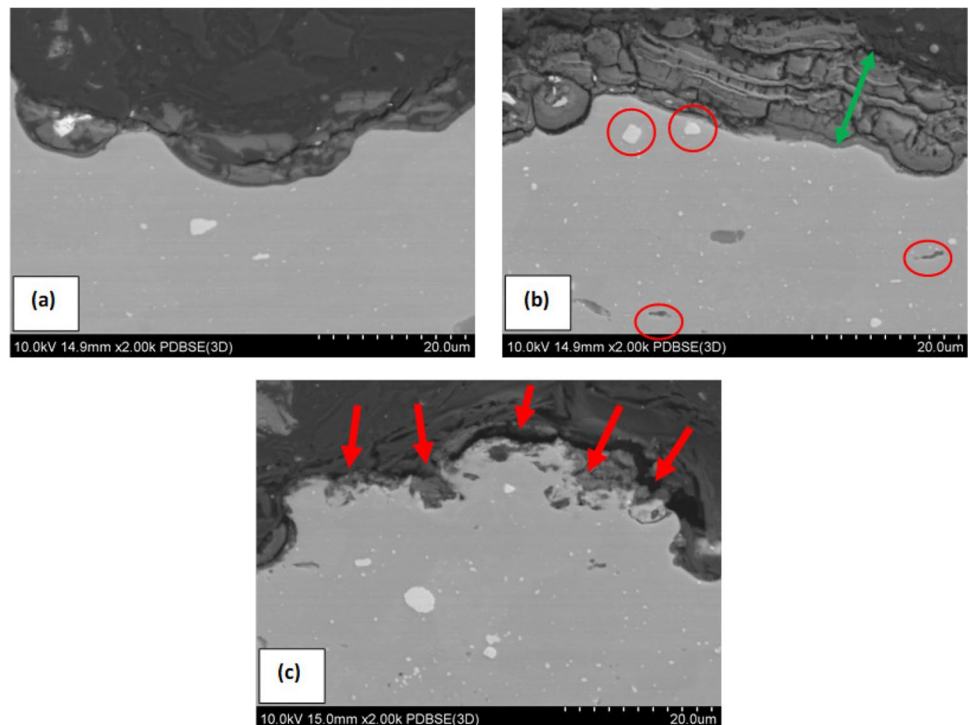
**Fig. 3** Dogbone specimen thickness reduction due to the HCC process

those specimens is more susceptible to hydrogen-induced blistering effects.

Figure 4 a–c illustrate near surface scanning electron micrographs of specimens A13 (no FSP / 80 mA/cm<sup>2</sup>), A23 (3-FSP passes / 80 mA/cm<sup>2</sup>), and A33 (8 FSP passes / 80 mA/cm<sup>2</sup>). The higher magnification of scanning electron images revealed significant surface defects for the 8 FSP passes hydrogen-charged specimens. More specifically, micro-cracks and voids are present in the surface area (see red arrows in Fig. 4c). The intense microstructural surface modification of the 8 FSP passes in combination with the harsh values of 80 mA/cm<sup>2</sup> HCC current density introduced surface defects in the specimens. Those defects increased the hydrogen diffusion in the metallic structure and consequently led to the degradation of the mechanical properties of the specimen that was observed in the mechanical characterization of the dogbone specimens.

Specimen A23 was further examined through EDS mapping analysis. Figure 5 shows the EDX elemental mapping analysis for the SEM image of Fig. 4b. Two different types of intermetallic compounds (IMCs) can be distinguished in the microstructure: brighter IMCs and darker IMCs (see Fig. 5b, red indicating circles). The color difference between the two types of IMCs is attributed to the differences in atomic weights caused by the different stoichiometric compositions. The elemental distribution profile obtained by the mapping technique shows that the brighter compounds are rich in Al and Fe. In addition, the dark compounds are rich in Mg and Si.

**Fig. 4** Scanning electron micrographs of specimen: **a** as-received without FSP and 80 mA/cm<sup>2</sup> HCC current density (A13); **b** 3 FSP passes and 80 mA/cm<sup>2</sup> HCC current density (A23); **c** 8 FSP passes and 80 mA/cm<sup>2</sup> HCC current density (A33)





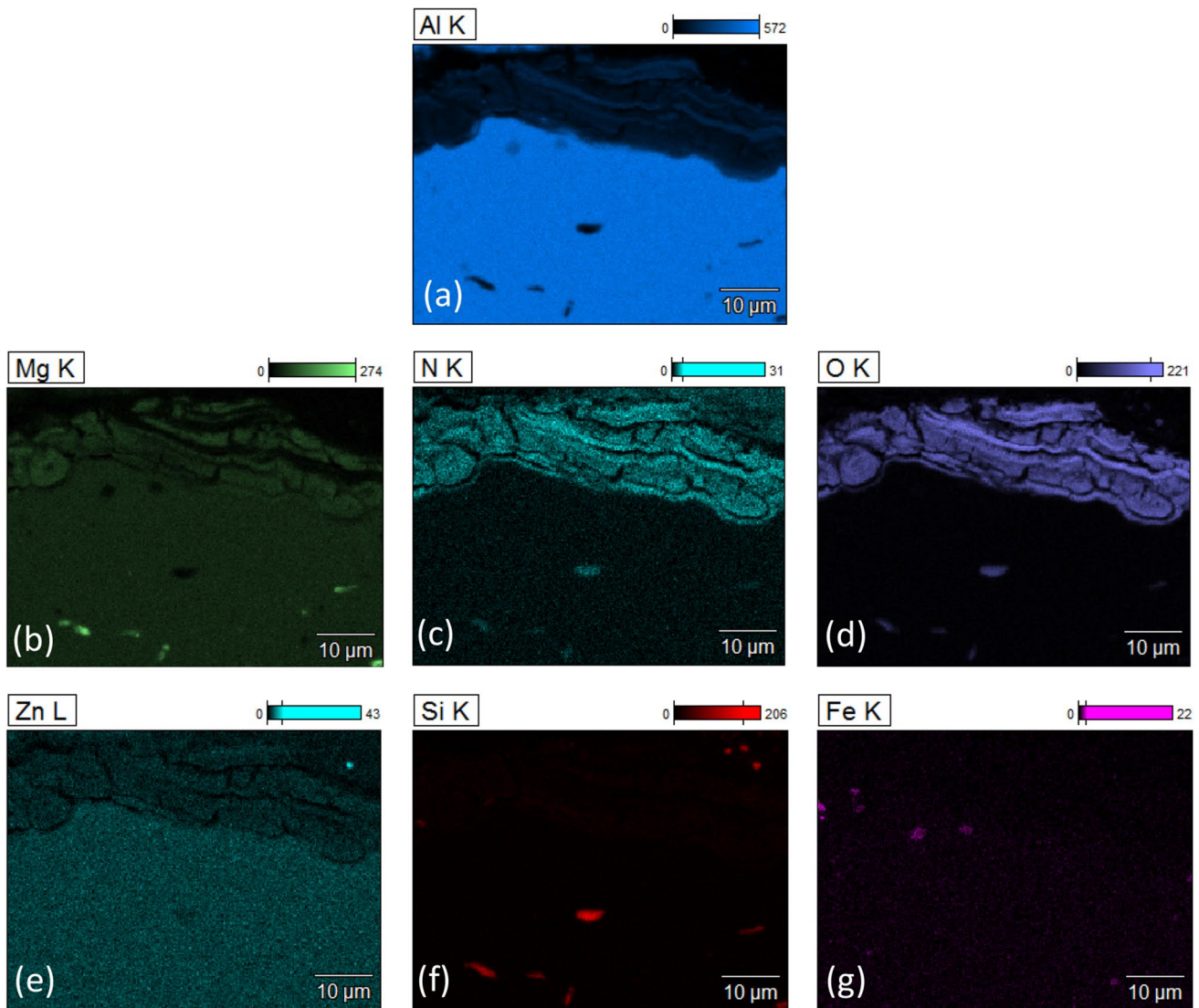


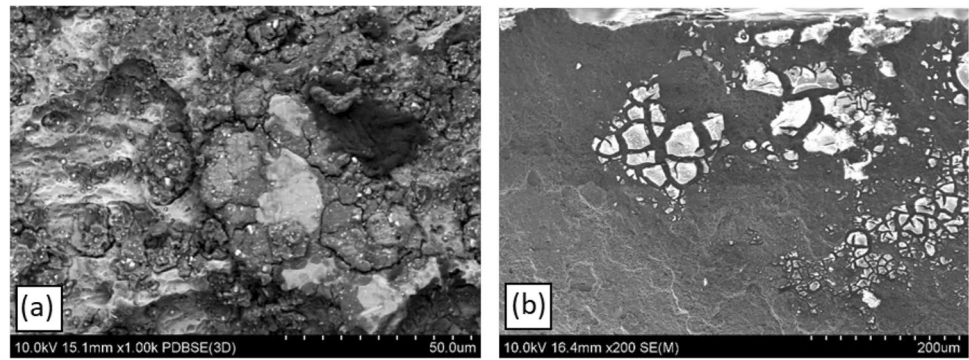
**Fig. 5** Energy-dispersive X-ray spectroscopy (EDX) mapping: **a** Al; **b** Mg; **c** N; **d** O; **e** Zn; **f** Si; **g** Fe

Furthermore, a non-cohesive scale has formed on the surface of the specimens (visible as a black layer—green arrow in Fig. 5b) as a product of the reaction between the test material and the corrosive environment. This scale is not uniformly distributed over the surface of the test specimens. The scale varies in thickness depending on where it is observed. The mapping analysis revealed that the layer is rich in Al, Mg, O, N, Zn, and Fe. The presence of N can be attributed to chemical reactions involving the ammonium thiocyanate ( $\text{NH}_4\text{SCN}$ ).

Observations of the surface of samples after the HCC test show large variations in the morphology of the formed scale. Figure 6 shows a typical surface of the sample after 8 FSP passes and  $80 \text{ mA/cm}^2$ . As seen in Fig. 6a, the scale forms “islands” and does not completely cover the surface of the samples. On the other hand, it forms a thick oxidation layer

on the surface. Additionally, as can be seen from Fig. 4a, numerous micro-cracks appear in the surface scale from the elongated blisters. Their presence can facilitate the formation of corrosion centers that could penetrate into the material. This phenomenon can be described based on the electrokinetic model of chloride solutions, incorporating chloride ion adsorption on oxide surfaces. In other words, the chloride ions penetrate deeper into the aluminum material through the oxidation film, followed by a localized dissolution of aluminum at the metal/oxide interface as a result of consecutive one-electron transfer reactions (as can be seen in Fig. 6b) [42]. During corrosion pit propagation, localized reactions produce an acidic environment below the oxide film, leading to blister formation. As hydrogen gas forms in the occluded corrosion cell, the blisters rupture [43]. The corrosion process in aluminum alloys is generally

**Fig. 6** Surface of the 8 pass FSPed specimens and subsequently given the corrosive environment conditions with 80 mA/cm<sup>2</sup> current density, **a** surface of the sample and **b** cross-section of the fracture zone



of a local nature because anodic and cathodic reactions are well-separated, and solution resistance limits the galvanic cell size [44].

### 3.2 Mechanical characterization

Through multi-pass FSP, grain refinement increases work hardening, yield, and ultimate tensile strength [23]. The interaction between dislocations and grain boundaries makes grain refinement highly effective at strengthening and stabilizing the microstructure [45, 46]. In other words, the tensile strength ( $R_m$ ) for samples without HE increased from 321 MPa for the base material to 336 MPa after 8 FSP passes. According to Fig. 7, the  $R_m$  drops after HE; for example, after 8 passes, the  $R_m$  drops from 336 to 285.7 MPa after 80 mA/cm<sup>2</sup> HCC. Although, in the case of the samples, after 3 FSP passes, the higher  $R_m$  drops from 336 MPa for the uncharged sample to 323 MPa after 50 mA/cm<sup>2</sup> HCC.

Typical stress-strain curves of the as-received and hydrogen-charged dogbone specimens with and without FSP are presented in Fig. 7. The energy absorption and the yield strength values are illustrated in the form of plots in Fig. 8 for the better evaluation of the results. More specifically, the plots of Fig. 8 a and b better highlight the effect of the FSP passes in different charging conditions whereas the plots of Fig. 8 c and d better highlight the effect of the charging conditions in specimens with different FSP passes (and the as-received material—no FSP).

A characteristic feature of the tension curves is the occurrence of instabilities and irregularities in the tension curves; this is the so-called Portevin-Le Chatelier (PLC) effect [47]. The band types are associated with the spatio-temporal organization of dislocations in the effective gage of a specimen and are assigned as type A, B, or C [48–50]. C-band types are randomly nucleated, non-propagating, or hopping bands across the width of the sample. They correspond to a tensile test curve with relatively consistent serrations around

**Fig. 7** Tensile testing stress-strain diagrams

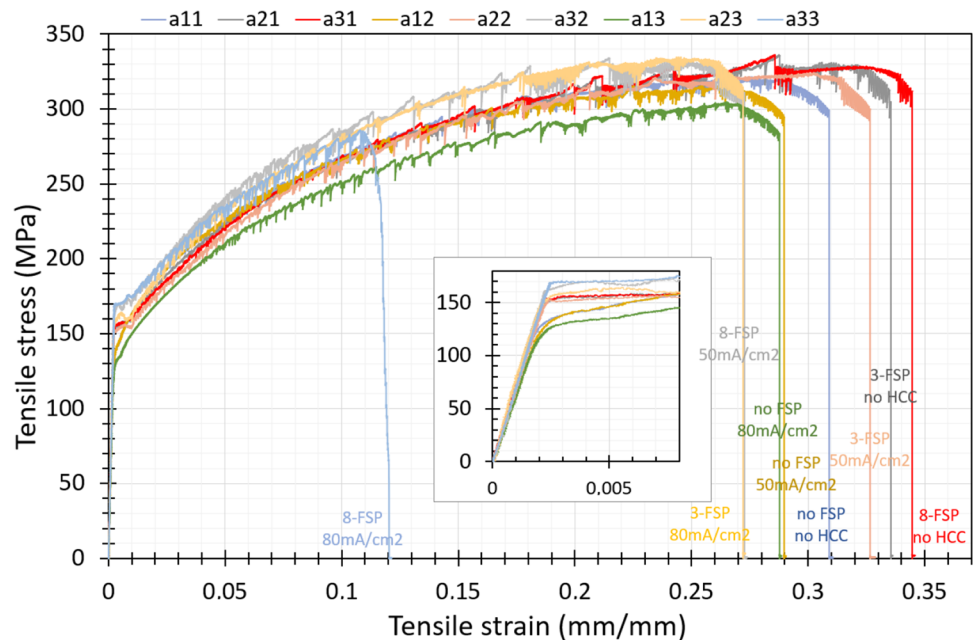
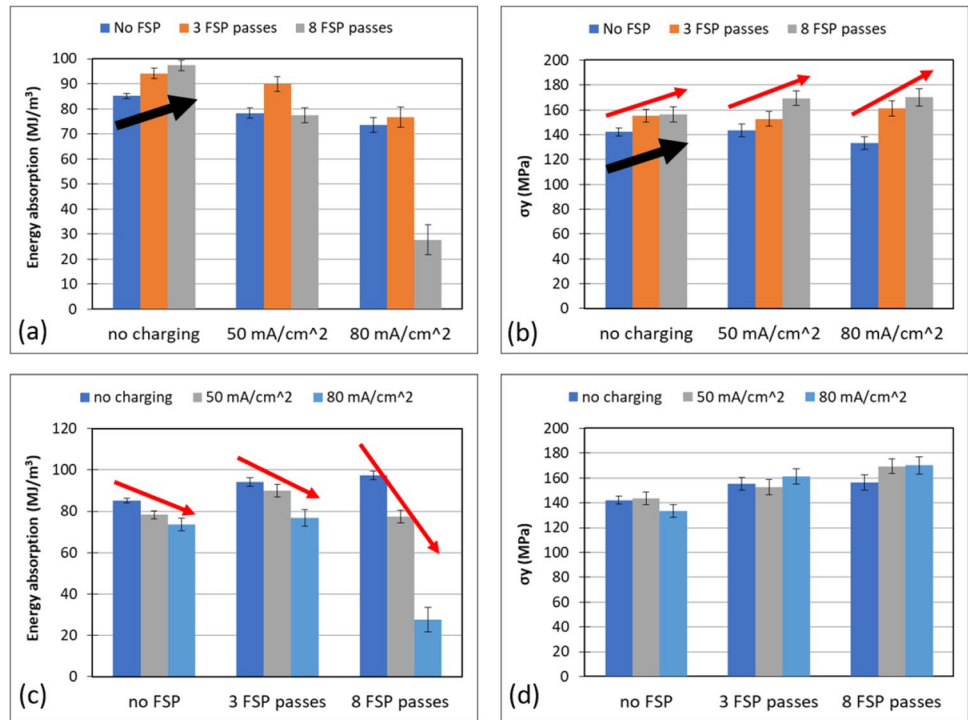




**Fig. 8** Effect of the FSP passes in different charging conditions for **a** the tensile energy absorption and **b** the yield strength. Effect of the charging conditions in specimens with different FSP passes for **c** the tensile energy absorption and **d** the yield strength



a given amplitude and frequency. B-band types, on the other hand, propagate intermittently in the gage at approximately equal intervals. The amplitudes and frequencies in the corresponding tensile test curve appear somewhat irregular and are smaller than those of the type C curve. Type A bands propagate continuously in a meter resembling a longitudinal wave, with arbitrarily placed small stress drops embedded in a regular flow. The sequential emergence of type A and type B bands has been observed in Al–Mg alloys [51].

The first main clear outcome from the plots of Fig. 8 a and b is that the FSP process introduced improved mechanical response in the aluminum alloy (in respect with the as-received specimen); the energy absorption was found increased from 85 MJ/m<sup>3</sup> of the base material to 94 MJ/m<sup>3</sup> and 97 MJ/m<sup>3</sup> for the 3 and 8 FSP passes, respectively.

The 5000 series grades of aluminum are non-heat treatable alloys; the temper is attained by the material being fully annealed and then rolled to the needed temper instead of being heat-treated. Therefore, the FSP process did not introduce any softening effects. On the other hand, the FSP process led to a significant grain refinement (Section 3.1) and this microstructural refinement introduced slightly increased energy absorption and yield strength (see black arrows of Fig. 8a, b).

Now, as for the effect of the hydrogen in the specimens, by examining Fig. 8b we can see that the yield strength has a clear trend to increase by increasing the FSP passes from 0 (base material) to 8 in all the HCC conditions (see red arrows in Fig. 8b). On the other hand, by examining Fig. 8d

we can reach to the conclusion that there is no significant effect in the yield strength caused by the HCC process. Thus, the HCC process does not appear to alter the yield strength of the as-received and FSPed materials.

Figure 8c presents the effect of the charging conditions on the energy absorption response of the specimens. The HCC appears to have a small effect (reduced energy absorption) on the as-received specimens (no FSP), where this effect appears slightly more intense in the 3-pass FSPed specimens and highly intense in the 8-pass FSPed specimens (see red arrows in Fig. 8d). More specifically, the energy absorption of the 8 FSP passes specimen dropped by 20% and 71% for the two different charging current densities. The 3 FSP passes specimen presented a reduction of 4% and 18%, respectively, where the base material presented a reduction of 8% and 14%, respectively.

The energy absorption was affected by the HCC process, and this is a clear indication of the presence of hydrogen in the aluminum matrix either in the form of hydrides, either diffused in the aluminum matrix or positioned in microstructural trapping sites. The presence of hydrogen could lead to the creation of micro-defects and the formation of micro-cracks, which degrade the mechanical properties of the material. Furthermore, the small cross-section and length of the specimens along with the defects could lead to premature failure and thus lower energy absorption values during the tensile testing experiments.

The 8-pass FSP specimens despite the slightly improved mechanical response with respect to the 3 FSP pass

specimens appears to be significantly affected by the HCC process. On the other hand, the 3 FSP pass specimens present similar response to the HCC process with the as-received material. To sum up, it is safe to say that the 3-pass FSP specimens presented the highest and more balanced values for energy absorption and yield strength in all HCC conditions, with respect to the as-received specimens and the 8-pass FSP specimens (Fig. 8a, b).

### 3.3 Microhardness distribution analysis

An increase in the number of passes results in the grain refinement, causing an increase in microhardness. The microhardness of the alloy after FSP modification increased compared to the starting material and was respectively  $82 \pm 0.5$  HV0.1 for the starting material,  $86 \pm 1$  HV0.1 for the material after 3 FSP passes, and  $90 \pm 0.8$  HV0.1 for the material after the processing with 8 passes. The increase in hardness after FSP treatment is mainly determined by grain refinement. Materials with small grain size have a higher fraction of grain boundaries, compared to coarse-grained materials. Grain boundaries affect strengthening, not least because they act as a barrier in the path of moving dislocations. For polycrystalline

materials with grain sizes above  $1 \mu\text{m}$ , the relationship between yield stress and the reciprocal of the square root of the grain size is captured by the Hall-Petch relationship. For grain sizes smaller than  $1 \mu\text{m}$ , the strength parameters are less dependent on the grain size, and the Hall-Petch relationship is often reversed [52, 53].

The research described in [54, 55] interrelates the corrosion rate with hardness of the aluminum alloy. The results show that the higher the hardness of the alloy is, the higher the hydrogen charging rate. Figure 9 shows the cross-section microhardness examination of the samples with and without HE as well as different multi-pass FSP stages. The examination revealed the surface hardening of the hydrogen-charged specimens but additionally increased by the number of passes. It is possible to explain the effect of HE on the increase of the surface hardness due to the dislocation phenomenon that occurs during the pinning mechanism [31, 56]. Based on the fundamental work of Fukai and Kuma [57], recent research [55] has shown that hydrogen atoms in interstitial positions stabilize vacancies by interacting with them. Deformation increases the number of hydrogen-vacancy complexes, which agglomerate over time and form nanovoids [58]. The presence of these defects causes the alloy to strain and harden, increasing its surface hardness in

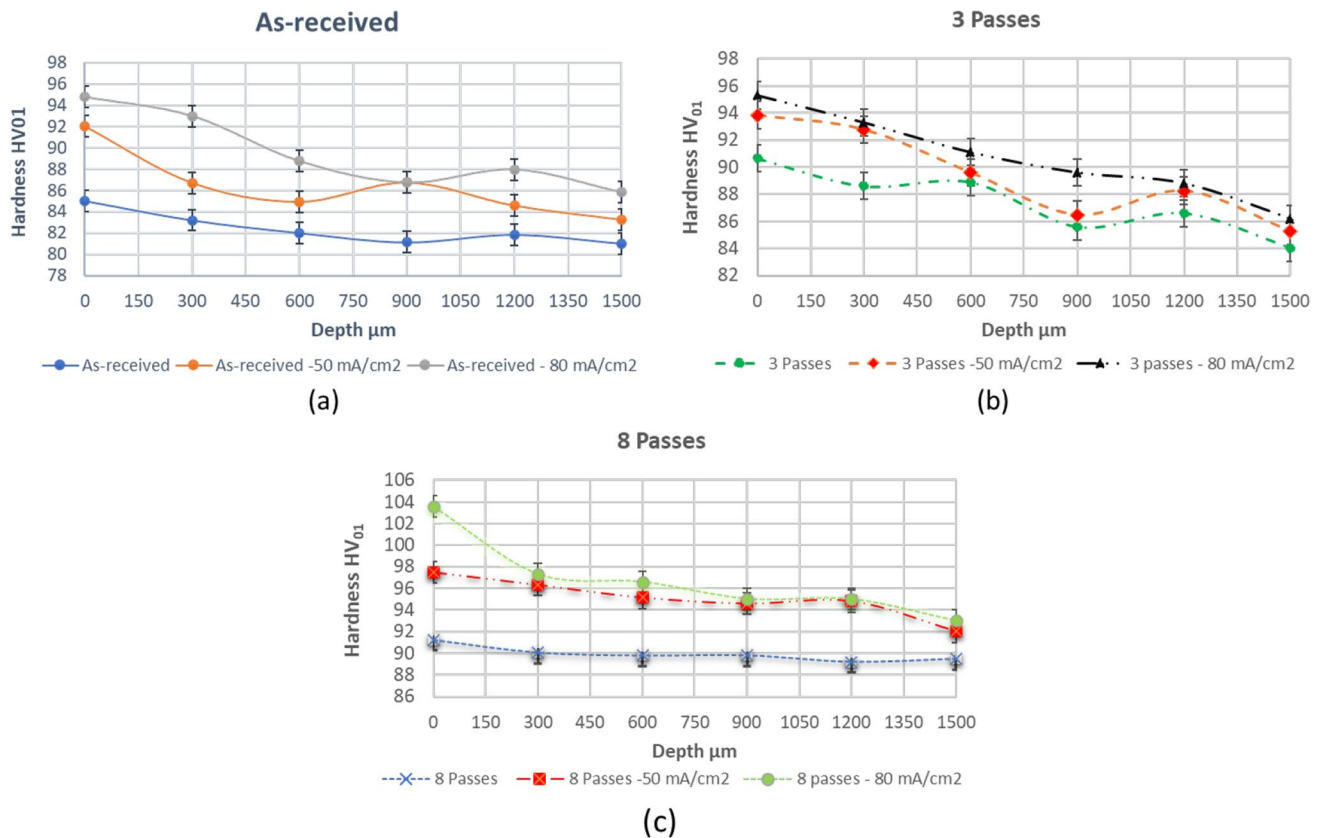


**Fig. 9** Microhardness depth analysis for **a** as-received samples, **b** 3 Passes, and **c** 8 passes with and without HE

the process. Additionally, there is a mechanism that is commonly observed for HE called hydrogen-enhanced localized plasticity (HELP). In the presence of solute atoms, dislocations have enhanced mobility, which Beachem first proposed [59]. As a result, less stress is required to move the dislocations. A HELP theory suggests that hydrogen solute atoms are often dislocation pinning sites because they localize dislocation density and pile up dislocations [60, 61].

By analyzing the microhardness of the samples (without FSP), it can be observed that the surface hardness increases after HE from 8.2% using 50 mA/cm<sup>2</sup> up to 13% using 80 mA/cm<sup>2</sup>. Based on the examinations of the samples in-depth, it was found that the surface hardness increases with a downward trend as the depth of the material is increased, as seen in Fig. 9 by comparing non-HE-charged samples with the charged ones. The hydrogen concentration in the higher layers is probably the cause of this increase in surface hardness. Additionally, by comparing the as-received materials with the others that undergo FSP in Fig. 9 a–c, it can be seen that by increasing the number of passes, the material increases its hardness. On top of that, by charging the FSP samples with hydrogen, the hardness of the samples increases too. The surface hardness of the 80 mA/cm<sup>2</sup> charged remains almost unchanged between the as-received material and the 3 passes. However, it increases from 96 to 104 HV<sub>0.1</sub> in the case of the 8 FSP passes compared to the abovementioned samples. This could be attributed to the higher number of dislocations and vacancies created by increasing the number of passes. As a result of these defects, hydrogen atoms can diffuse along these pathways and can be trapped at these sites, thereby accelerating the process of hydrogen uptake.

### 3.4 Fracture analysis

Scanning electron and 3D FVM digital microscopy technique were applied for the characterization of the fractured surfaces of the dogbone specimens. Figure 2 shows the surface macro- and microtopology of the tested samples. Specifically Fig. 10 a, c, e, g, i, and k present the surface topology 3D macrographs, whereas Fig. 10 b, d, f, h, j, and l present SEM micrographs of higher magnification. The fractures of the investigated materials, both before and after the FSP process, have a ductile transcrystalline character; it is characterized by significant unevenness of the interface. This type of fracture occurs when the cohesive strength in the crystallographic planes located in the direction of the fracture is greater than the slip stress in the planes that intersect the direction of the fracture [62]. Voids are generated and enlarged during the plastic deformation of alloys and then coalesce to generate cracks. Coalescence occurs as a result of the expansion of voids, followed by the elongation of the material connections between the voids. Second-phase

particles such as precipitations are considered to be the initial sites of void formation; however, voids can also form around dislocation loops [63–65].

By comparing the topography of the as-received specimen with no HCC (Fig. 10a, b) with the 3 FSP passes specimen (Fig. 10c, d) and the 8 FSP passes specimen also without HCC (Fig. 10e, f), we can see that the as-received specimen presents a rougher surface with larger dimples but uniformly distributed in the fractured surface. On the other hand, the FSPed specimens present smoother surfaces with smaller dimples; this can be correlated to the refined microstructure of the specimens and the enhanced mechanical response in the tension testing experiments. Furthermore, the FSPed specimens introduced an asymmetrical surface failure appearance (Fig. 10 c and e—see black arrows) with respect to the as-received specimen (Fig. 10a). This can be attributed to the intense plastic deformation phenomena and the asymmetrical straining that take place during the intense stirring action of the FSP process. We could say that the obtained nugget-type stir zone leads to microscopically anisotropic properties.

The HCC process on the as-received specimen does not appear to significantly alter the surface topography. On the other hand, the 3 and 8 FSP passes specimens presented a similar fracture topography; the fracture appears to develop from the outer surface (Fig. 10 i and k—see red arrows). This can be attributed to surface microstructural phenomena driven from the presence of hydrogen. This means that the weakened surface led to intense straining that in the case of the 8 FSP passes specimens led to premature failure.

## 4 Conclusions

In the present work, FSPed specimens with different numbers of FSP passes were subjected to intense hydrogen cathodic charging using different charging current densities. Charged and uncharged specimens were then subjected to extensive mechanical and microstructural characterization.

The FSP process introduced a refined microstructure with finer grains. This led to an improved mechanical response during tension tests of the uncharged specimens; the energy absorption increased from 85 MJ/m<sup>3</sup> of the base material to 94 MJ/m<sup>3</sup> and 97 MJ/m<sup>3</sup> for the 3 and 8 FSP passes, respectively. For the 8 FSP passes hydrogen-charged specimens, the microstructural characterization revealed significant surface defects. Those defects increased the hydrogen diffusion in the metallic structure and consequently led to the degradation of the mechanical properties of the specimens. Thus, the introduction of hydrogen through the HCC process led to a more brittle mechanical response with a decrease in the energy absorption capability for all the specimens.



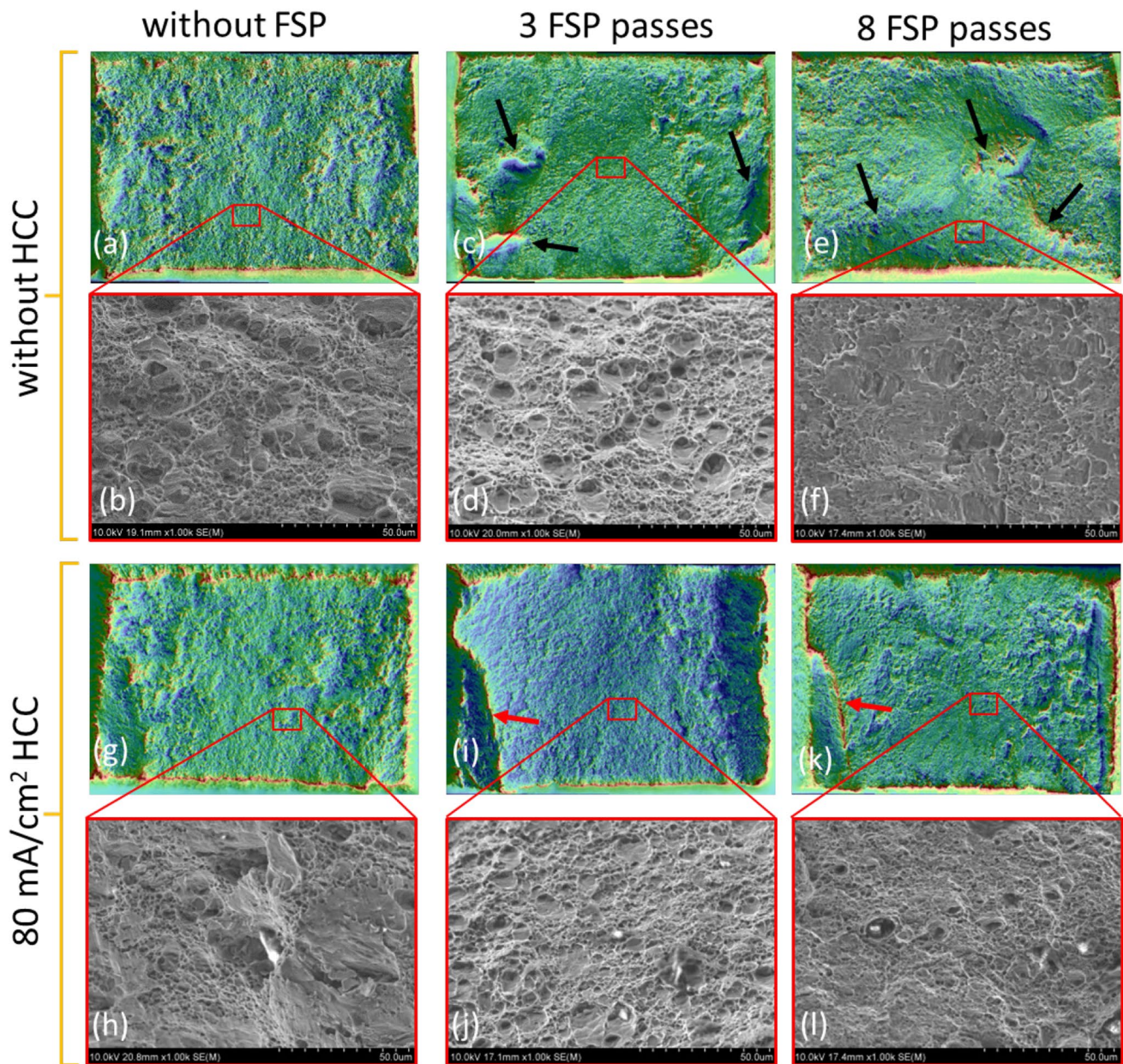


**Fig. 10** Surface topology 3D macrographs and SEM micrographs of: **a, b** as-received (A11), **c, d** 3 FSP passes and without HCC (A21), **e, f** 8 FSP passes and without HCC (A31), **g, h** as-received without FSP

and 80 mA/cm<sup>2</sup> HCC current density, **i, j** 3 FSP passes and 80 mA/cm<sup>2</sup> HCC current density (A23), **k, l** 8 FSP passes and 80 mA/cm<sup>2</sup> HCC current density (A33)

The energy absorption for the specimen with the 8 FSP passes dropped by 20% and 71% for the two different charging current densities, respectively. The 3 FSP passes specimen presented a reduction of energy absorption of 4% and 18%, whereas the as-received material presented a reduction of 8% and 14%, respectively (for the 50 and 80 mA/cm<sup>2</sup> charging current densities). This brittle response is also evident from the microhardness testing results where the examination presented a surface hardening effect for the hydrogen-charged specimens

that was additionally affected (increased) by the number of FSP passes. The specimens with no FSP presented the lower reduction of the energy absorption values. Nevertheless, the refined microstructure of the 3 FSP specimens led to a slightly higher energy absorption decrease, where the 8 FSP passes specimens presented a significantly higher energy absorption reduction. This trend is also evident through the microhardness evaluation analysis (higher hardness profiles) and also through the thickness reduction values of the dogbone

specimens; the thickness reduction was caused by the intense surface blistering effects.

To conclude, the 3 FSP passes specimen, despite the slightly higher reduction of energy absorption (with respect to the as-received specimen), in pure numbers, presented a better mechanical response. Furthermore, the 8 FSP passes specimens, despite the slightly better mechanical response in the non-charged specimens, in an industrial point of view, would not be cost-effective. Here, we must also mention that the HCC parameters were significantly intense (charging current density and time). From the above, we could reach to the conclusion that a small number FSP surface modification improves the mechanical response of the specific aluminum alloy (AA5083) and is not significantly affected by hydrogen charging environments.

The present paper was focused on the impact of the FSP process on hydrogen susceptibility of AA5083 specimens after intense hydrogen cathodic charging. The effect of the HCC process was examined through mechanical testing and the results were correlated to microstructural investigation analysis. Future work concerns further and deeper understanding of the involving mechanisms by detailed characterization and evaluation of the microstructure after the FSP process, carried out under different conditions using a variety of research techniques, including EBSD and transmission electron microscopy.

**Author contribution** I.P. and P.K.O. carried out the experiments and formal analysis of the original draft, while D.M. and B.L.M., as supervisors, discussed the methods and conclusions, and provided the final review and editing. Finally, all authors reviewed the paper.

**Funding** Funded by the Basic Research Program PEVE 2020 of the National Technical University of Athens. Open access funding provided by HEAL-Link Greece.

## Declarations

**Ethical approval** Not applicable.

**Conflict of interest** The authors declare no competing interests.

**Open Access** This article is licensed under a Creative Commons Attribution 4.0 International License, which permits use, sharing, adaptation, distribution and reproduction in any medium or format, as long as you give appropriate credit to the original author(s) and the source, provide a link to the Creative Commons licence, and indicate if changes were made. The images or other third party material in this article are included in the article's Creative Commons licence, unless indicated otherwise in a credit line to the material. If material is not included in the article's Creative Commons licence and your intended use is not permitted by statutory regulation or exceeds the permitted use, you will need to obtain permission directly from the copyright holder. To view a copy of this licence, visit <http://creativecommons.org/licenses/by/4.0/>.

## References

1. Mirzadeh H (2021) High strain rate superplasticity via friction stir processing (FSP): a review. *Mater Sci Eng A* 819:141499. <https://doi.org/10.1016/j.msea.2021.141499>
2. Harwani D, Badheka V, Patel V, Li W, Andersson J (2021) Developing superplasticity in magnesium alloys with the help of friction stir processing and its variants – a review. *J Mater Res Technol* 12:2055–2075. <https://doi.org/10.1016/j.jmrt.2021.03.115>
3. Barooni O, Abbasi M, Givi M et al (2017) New method to improve the microstructure and mechanical properties of joint obtained using FSW. *Int J Adv Manuf Technol* 93:4371–4378. <https://doi.org/10.1007/s00170-017-0810-3>
4. Papantoniou IG, Kyriakopoulou HP, Pantelis DI et al (2018) Manufacturing process of AA5083/nano- $\gamma$ Al<sub>2</sub>O<sub>3</sub> localized composite metal foam fabricated by friction stir processing route (FSP) and microstructural characterization. *J Mater Sci* 53:3817–3835. <https://doi.org/10.1007/s10853-017-1802-2>
5. Papantoniou IG, Kyriakopoulou HP, Pantelis DI et al (2018) Fabrication of MWCNT-reinforced Al composite local foams using friction stir processing route. *Int J Adv Manuf Technol* 97:675–686. <https://doi.org/10.1007/s00170-018-1964-3>
6. Ma Z (2008) Friction stir processing technology: a review. *Metall Mater Trans A* 39:642–658. <https://doi.org/10.1007/s11661-007-9459-0>
7. Węglowski MS (2017) Friction stir processing – state of the art. *Arch Civil Mech Eng* 18:114–129. <https://doi.org/10.1016/j.acme.2017.06.002>
8. Paz Martínez-Viademonte M, Abrahamsi ST, Hack T, Burchardt M, Terryn H (2020) A review on anodizing of aerospace aluminum alloys for corrosion protection. *Coatings* 10(11):1106. <https://doi.org/10.3390/coatings10111106>
9. Mishra RS, Mahoney MW, McFadden SX, Mara NA, Mukherjee AK (1999) High strain rate superplasticity in a friction stir processed 7075 Al alloy. *Scr Mater* 42:163–168. [https://doi.org/10.1016/S1359-6462\(99\)00329-2](https://doi.org/10.1016/S1359-6462(99)00329-2)
10. Johannes LB, Mishra RS (2007) Multiple passes of friction stir processing for the creation of superplastic 7075 aluminum. *Mater Sci Eng A* 464:255–260. <https://doi.org/10.1016/j.msea.2007.01.141>
11. Yadav D, Bauri R (2012) Effect of friction stir processing on microstructure and mechanical properties of aluminium. *Mater Sci Eng A* 539:85–92. <https://doi.org/10.1016/j.msea.2012.01.055>
12. Gan WY, Zhou Z, Zhang H, Peng T (2014) Evolution of microstructure and hardness of aluminum after friction stir processing. *Trans Nonferrous Met Soc Chin* 24:975–981. [https://doi.org/10.1016/S1003-6326\(14\)63151-4](https://doi.org/10.1016/S1003-6326(14)63151-4)
13. Senthilkumar R, Prakash M, Arun N, Jeyakumar AA (2019) The effect of the number of passes in friction stir processing of aluminum alloy (AA6082) and its failure analysis. *Appl Surf Sci* 491:420–431. <https://doi.org/10.1016/j.apsusc.2019.06.132>
14. Patel V, Badheka V, Kumar A (2017) Effect of polygonal pin profiles on friction stir processed superplasticity of AA7075 alloy. *J Mater Process Technol* 240:68–76. <https://doi.org/10.1016/j.jmatp.2016.09.009>
15. Wang BB, Wu LH, Xue P, Ni DR, Xiao BL, Liu YD, Ma ZY (2020) Improved high cycle fatigue property of ultrafine grained pure aluminum. *Mater Lett* 277:128289. <https://doi.org/10.1016/j.matlet.2020.128289>
16. Nelaturu P, Jana S, Mishra RS, Grant G, Carlson BE (2020) Effect of temperature on the fatigue cracking mechanisms in A356 Al alloy. *Mater Sci Eng A* 780:139175. <https://doi.org/10.1016/j.msea.2020.139175>



17. Wang BB, Xie GM, Wu LH, Xue P, Ni DR, Xiao BL, Liu YD, Ma ZY (2021) Grain size effect on tensile deformation behaviors of pure aluminum. *Mater Sci Eng A* 820:141504. <https://doi.org/10.1016/j.msea.2021.141504>
18. Bagheri B, Abdollahzadeh A, Sharifi F, Abbasi M, Moghaddam AO (2021) Recent development in friction stir processing of aluminum alloys: microstructure evolution, mechanical properties, wear and corrosion behaviors. *Proc Inst Mech Eng Pt C J Mechan Eng*. <https://doi.org/10.1177/09544089211058007>
19. Bagheri B, Abdollahzadeh A, Abbasi M et al (2021) Effect of vibration on machining and mechanical properties of AZ91 alloy during FSP: modeling and experiments. *Int J Mater Form* 14:623–640. <https://doi.org/10.1007/s12289-020-01551-2>
20. Abbasi M, Bagheri B, Sharifi F (2021) Simulation and experimental study of dynamic recrystallization process during friction stir vibration welding of magnesium alloys. *Trans Nonferrous Met Soc Chin* 31:2626–2650. [https://doi.org/10.1016/S1003-6326\(21\)65681-9](https://doi.org/10.1016/S1003-6326(21)65681-9)
21. Nagumo M (2016) Solid solution. *Fundamentals of Hydrogen Embrittlement*. Springer, Singapore. [https://doi.org/10.1007/978-981-10-0161-1\\_1](https://doi.org/10.1007/978-981-10-0161-1_1)
22. Su H, Toda H, Shimizu K, Uesugi K, Takeuchi A, Watanabe Y (2019) Assessment of hydrogen embrittlement via image-based techniques in Al–Zn–Mg–Cu aluminum alloys. *Acta Mater* 176:96–108. <https://doi.org/10.1016/j.actamat.2019.06.056>
23. Safyari M, Moshtaghi M, Hojo T, Akiyama E (2022) Mechanisms of hydrogen embrittlement in high-strength aluminum alloys containing coherent or incoherent dispersoids. *Corros Sci* 194:109895. <https://doi.org/10.1016/j.corsci.2021.109895>
24. Louthan MR, Caskey GR, Donovan JA, Rawl DE (1972) Hydrogen embrittlement of metals. *Mater Sci Eng A* 10:357–368. [https://doi.org/10.1016/0025-5416\(72\)90109-7](https://doi.org/10.1016/0025-5416(72)90109-7)
25. Takano N (2008) Hydrogen diffusion and embrittlement in 7075 aluminum alloy. *Mater Sci Eng A* 483–484:336–339. <https://doi.org/10.1016/j.msea.2006.08.144>
26. Lee D, Nishikawa H, Oda Y et al (2013) Small fatigue crack growth characteristics and fracture surface morphology of low carbon steel in hydrogen gas. *Int J Fract* 179:147–156. <https://doi.org/10.1007/s10704-012-9783-2>
27. Kumar S, Nambodhiri TKG (2011) Precipitation hardening and hydrogen embrittlement of aluminum alloy AA7020. *Bull Mater Sci* 34:311–321. <https://doi.org/10.1007/s12034-011-0066-8>
28. Scully JR, Young GA, Smith SW (2012) 19 - Hydrogen embrittlement of aluminum and aluminum-based alloys. *Woodhead Publ Ser Met Surf Eng* 2:707–768. <https://doi.org/10.1533/9780857093899.3.707>
29. Troiano AR (2016) The role of hydrogen and other interstitials in the mechanical behavior of metals. *Metallogr Microstruct Anal* 5:557–569. <https://doi.org/10.1007/s13632-016-0319-4>
30. Oriani RA (1970) The diffusion and trapping of hydrogen in steel. *Acta Metall* 18:147–157. [https://doi.org/10.1016/0001-6160\(70\)90078-7](https://doi.org/10.1016/0001-6160(70)90078-7)
31. Georgiou EP, Celis JP, Panagopoulos CN (2017) The effect of cold rolling on the hydrogen susceptibility of 5083 aluminum alloy. *Metals* 7(11):451. <https://doi.org/10.3390/met7110451>
32. Vasco MC, Tserpes K, Pantelakis SG (2018) Numerical simulation of tensile behavior of corroded aluminum alloy 2024 T3 considering the hydrogen embrittlement. *Metals* 8(1):56. <https://doi.org/10.3390/met8010056>
33. Safyari M, Moshtaghi M, Kuramoto S (2021) On the role of traps in the microstructural control of environmental hydrogen embrittlement of a 7xxx series aluminum alloy. *J Alloys Compd* 855:157300. <https://doi.org/10.1016/j.jallcom.2020.157300>
34. Chen RY, Chu HY, Lai CC, Wu CT (2015) Effects of annealing temperature on the mechanical properties and sensitization of 5083-H116 aluminum alloy. *Proc Inst Mech Eng L: J Mater Des Appl* 229(4):339–346. <https://doi.org/10.1177/1464420713512249>
35. Gangil N, Maheshwari S, Siddiquee AN (2018) Multipass FSP on AA6063-T6 Al: strategy to fabricate surface composites. *Mater Manuf Proc* 33:805–811. <https://doi.org/10.1080/10426914.2017.1415448>
36. ASTM G148–97 Standard practice for evaluation of hydrogen uptake, permeation, and transport in metals by an electrochemical technique (2011)
37. Mishra RS, Ma ZY, Charit I (2003) Friction stir processing: a novel technique for fabrication of surface composite. *Mater Sci Eng A* 341(1–2):307–310. [https://doi.org/10.1016/S0921-5093\(02\)00199-5](https://doi.org/10.1016/S0921-5093(02)00199-5) ISSN:0921–5093
38. Mishra RS, De PS, Kumar N (2014) *Friction stir welding and processing, science and engineering*. Springer International Publishing, Switzerland
39. McQueen HJ (2004) Development of dynamic recrystallization theory. *Mater Sci Eng A* 387–389:203–208
40. Huang K, Logé R (2016) A review of dynamic recrystallization phenomena in metallic materials. *Mater Des* 111:548–574
41. McQueen HJ, Blum W (2000) Dynamic recovery: sufficient mechanism in the hot deformation of Al (<99.99). *Mater Sci Eng A* A290:95–107
42. McCafferty E (2003) Sequence of steps in the pitting of aluminum by chloride ions. *Corros Sci* 45(7):1421–1438, ISSN 0010-938X. [https://doi.org/10.1016/S0010-938X\(02\)00231-7](https://doi.org/10.1016/S0010-938X(02)00231-7)
43. Ryan RL Rupture of an oxide blister. *J Electrochem Soc* 142(8):2594. <https://doi.org/10.1149/1.2050059>
44. Sukiman NL, Zhou X, Birbilis N, Mol JM, Garcia SJ, Zhou X, Thompson GE (2013) Durability and corrosion of aluminium and its alloys: overview, property space, techniques and developments. In: Ahmad Z (ed) *Book Aluminium alloys – new trends in fabrication and applications*. InTech, pp 47–97 ISBN 978-953-51-0861-0
45. Apps PJ, Berta M, Prangnell PB (2005) The effect of dispersoids on the grain refinement mechanisms during deformation of aluminium alloys to ultra-high strains. *Acta Mater* 53(2):499–511, ISSN 1359-6454. <https://doi.org/10.1016/j.actamat.2004.09.042>
46. Guan RG, Tie D (2017) A review on grain refinement of aluminum alloys: progresses, challenges and prospects. *Acta Metall Sin (Engl Lett)* 30:409–432. <https://doi.org/10.1007/s40195-017-0565-8>
47. Yilmaz A The Portevin–Le Chatelier effect: a review of experimental findings. *Sci Technol Adv Mater* 12(6):063001. <https://doi.org/10.1088/1468-6996/12/6/063001>
48. Schwink C, Nortmann A (1997) The present experimental knowledge of dynamic strain ageing in binary f.c.c. solid solutions. *Mater Sci Eng A* 234–236:1–7, ISSN 0921-5093. [https://doi.org/10.1016/S0921-5093\(97\)00139-1](https://doi.org/10.1016/S0921-5093(97)00139-1)
49. Chihab K, Estrin Y, Kubin LP, Vergnol J (1987) The kinetics of the Portevin–Le Chatelier bands in an Al-5at%Mg alloy. *Scripta Metallurgica* 21(2):203–208, ISSN 0036-9748. [https://doi.org/10.1016/0036-9748\(87\)90435-2](https://doi.org/10.1016/0036-9748(87)90435-2)
50. Hähner P (1996) On the physics of the Portevin–Le Châtelier effect part 2: from microscopic to macroscopic behaviour. *Mater Sci Eng A* 207(2):216–223, ISSN 0921-5093. [https://doi.org/10.1016/0921-5093\(95\)10032-6](https://doi.org/10.1016/0921-5093(95)10032-6)
51. Ait-Amokhtar H, Fressengeas C (2010) Crossover from continuous to discontinuous propagation in the Portevin–Le Chatelier effect. *Acta Mater* 58(4):1342–1349, ISSN 1359-6454. <https://doi.org/10.1016/j.actamat.2009.10.038>
52. Chinh N, Olasz D, Ahmed AQ, Sáfrán G, Lendvai J, Langdon TJ (2023) Modification of the Hall–Petch relationship for submicron-grained fcc metals. *Mater Sci Eng A* 862:144419. <https://doi.org/10.1016/j.msea.2022.144419>
53. Abbasi M, Abdollahzadeh A, Bagheri B, Ostovari Moghaddam A, Sharifi F, Dadaei M (2021) Study on the effect of the



- welding environment on the dynamic recrystallization phenomenon and residual stresses during the friction stir welding process of aluminum alloy. *Proc Inst Mech Eng L J Mater Des App* 235(8):1809–1826. <https://doi.org/10.1177/14644207211025113>
54. Panagopoulos C, Georgiou E (2007) The effect of hydrogen charging on the mechanical behaviour of 5083 wrought aluminum alloy. *Corros Sci* 49(12):4443–4451, ISSN 0010-938X. <https://doi.org/10.1016/j.corsci.2007.03.047>
55. Kamoutsi H, Haidemenopoulos GN, Bontozoglou V, Pantelakis S (2006) Corrosion-induced hydrogen embrittlement in aluminum alloy 2024. *Corros Sci* 48(5):1209–1224, ISSN 0010-938X. <https://doi.org/10.1016/j.corsci.2005.05.015>
56. Watson JW, Shen YZ, Meshii M (1988) Effect of cathodic charging on the mechanical properties of aluminum. *Metall Trans A* 19:2299–2304
57. Fukai Y, Okuma N (1993) Evidence of copious vacancy formation in Ni and Pd under high hydrogen pressure. *Jpn J Appl Phys* 32:1256–1259
58. Li S, Li Y, Lo YC, Neeraj T, Srinivasan R, Ding X, Sun J, Qi L, Gumbsch P, Li J (2015) The interaction of dislocations and hydrogen-vacancy complexes and its importance for deformation-induced proto nano-voids formation in  $\alpha$ -Fe. *Int J Plast* 74:175–191
59. Beachem C A new model for hydrogen-assisted cracking (hydrogen “embrittlement”). *Met Trans* 3(2):437–451
60. Robertson IM (2001) The effect of hydrogen on dislocation dynamics. *Eng Fract Mech* 68:671–692
61. Krasnikov V, Bezborodova P, Mayer A (2022) Effect of hydrogen accumulation on  $\theta'$  precipitates on the shear strength of Al-Cu alloys. *Int J Plast* 103475, ISSN 0749-6419. <https://doi.org/10.1016/j.ijplas.2022.103475>
62. French IE, Weestrch PF (1976) The shear mode of ductile fracture in materials with few inclusions. *Metall Mater Trans A* 7:1841–1845. <https://doi.org/10.1007/BF02659814>
63. Bagheri B, Abbasi M, Hamzeloo R (2020) The investigation into vibration effect on microstructure and mechanical characteristics of friction stir spot vibration welded aluminum: simulation and experiment. *Proc IMechE, C: J Mater Des Appl* 234:1809–1822
64. Bsgheri B, Abbasi M, Abdollahzadeh A, Mirsalehi S (2020) Effect of second-phase particle size and presence of vibration on AZ91/SiC surface composite layer produced by FSP. *Trans Non-ferrous Met Soc Chin* 30(4):905–916, ISSN 1003-6326. [https://doi.org/10.1016/S1003-6326\(20\)65264-5](https://doi.org/10.1016/S1003-6326(20)65264-5)
65. Abbasi M, Givi M, Bagheri B (2020) New method to enhance the mechanical characteristics of Al-5052 alloy weldment produced by tungsten inert gas. *Proc Inst Mech Eng B J Eng Manuf* 0(0). <https://doi.org/10.1177/0954405420929777>

**Publisher's note** Springer Nature remains neutral with regard to jurisdictional claims in published maps and institutional affiliations.